

Signal to Noise Ratio and Spectral Sampling Constraints on Olivine Detection and Compositional Determination in the Intermediate Infrared Region: Applications in Planetary Sciences

Sebastian Alonso Perez-Lopez¹, Christopher H Kremer¹, and John F Mustard¹

¹Brown University

December 14, 2023

Abstract

The intermediate infrared region (IMIR, 4 – 8 μm) provides significant advantages over the visible-shortwave infrared and mid-infrared for quantitative determination of mafic mineral composition. In particular, olivine's sharp spectral features in IMIR spectra exhibit systematic shifts in wavelength position with iron-magnesium content. Previous IMIR studies have used laboratory data, with signal-to-noise ratios (SNRs) and spectral resolutions greater than those expected of imaging spectrometers. Here we employ a feature fitting algorithm to quantitatively assess the influence of SNR and sampling rate on olivine detection and compositional interpretation from IMIR data. We demonstrate that olivine is easily distinguished from pyroxene and other lunar-relevant minerals across IMIR wavelengths, with the feature-fitting algorithm effectively determining olivine composition for various synthetic, terrestrial, Martian, and lunar samples with an average error of only 6.4 mol%. We then apply the feature-fitting routine to degraded spectra with reduced SNRs and sampling rates, establishing data-quality thresholds for accurate determination of olivine composition. Spectra for the sample most relevant to lunar exploration, an Apollo 74002 drive tube consisting of microcrystalline olivine and glass-rich pyroclastics, required SNRs [?] 200 for sampling rates [?] 25 nm to predict composition within ± 11 Mg# (molar $\text{Mg}/[\text{Mg}+\text{Fe}] * 100$) of the sample's true composition. Derived limits on SNRs and sampling rates will serve as valuable inputs for the development of IMIR imaging spectrometers, enabling comprehensive knowledge of olivine composition across the lunar surface and providing valuable insight into the Moon's crustal history and thermal evolution.

Hosted file

982151_0_art_file_11686851_s5mf5g.docx available at <https://authorea.com/users/709109/articles/693452-signal-to-noise-ratio-and-spectral-sampling-constraints-on-olivine-detection-and-compositional-determination-in-the-intermediate-infrared-region-applications-in-planetary-sciences>

1
2 **Signal to Noise Ratio and Spectral Sampling Constraints on Olivine Detection and**
3 **Compositional Determination in the Intermediate Infrared Region: Applications in**
4 **Planetary Sciences**
5

6 **S. A. Pérez-López¹, C. H. Kremer², and J. F. Mustard¹**

7 ¹Department of Earth, Environmental, and Planetary Sciences, Brown University, Providence,
8 RI, USA, ²Department of Geosciences, Stony Brook University, Long Island, NY, USA

9 Corresponding author: Sebastian Pérez-López (sebastian_perez-lopez@brown.edu)

10 **Key Points:**

- 11 • We use a feature fitting routine to predict olivine composition from degraded spectral
12 data in the intermediate infrared region (4 – 8 μm).
- 13 • Accurate prediction of olivine composition is observed at data qualities expected of
14 imaging spectrometers.

15 **Abstract**

16 The intermediate infrared region (IMIR, 4 – 8 μm) provides significant advantages over the
17 visible-shortwave infrared and mid-infrared for quantitative determination of mafic mineral
18 composition. In particular, olivine's sharp spectral features in IMIR spectra exhibit systematic
19 shifts in wavelength position with iron-magnesium content. Previous IMIR studies have used
20 laboratory data, with signal-to-noise ratios (SNRs) and spectral resolutions greater than those
21 expected of imaging spectrometers. Here we employ a feature fitting algorithm to quantitatively
22 assess the influence of SNR and sampling rate on olivine detection and compositional
23 interpretation from IMIR data. We demonstrate that olivine is easily distinguished from
24 pyroxene and other lunar-relevant minerals across IMIR wavelengths, with the feature-fitting
25 algorithm effectively determining olivine composition for various synthetic, terrestrial, Martian,
26 and lunar samples with an average error of only 6.4 mol%. We then apply the feature-fitting
27 routine to degraded spectra with reduced SNRs and sampling rates, establishing data-quality
28 thresholds for accurate determination of olivine composition. Spectra for the sample most
29 relevant to lunar exploration, an Apollo 74002 drive tube consisting of microcrystalline olivine
30 and glass-rich pyroclastics, required SNRs ≥ 200 for sampling rates ≤ 25 nm to predict
31 composition within ± 11 Mg# (molar $\text{Mg}/[\text{Mg}+\text{Fe}] * 100$) of the sample's true composition.
32 Derived limits on SNRs and sampling rates will serve as valuable inputs for the development of
33 IMIR imaging spectrometers, enabling comprehensive knowledge of olivine composition across
34 the lunar surface and providing valuable insight into the Moon's crustal history and thermal
35 evolution.

36 **Plain Language Summary**

37 An understanding of olivine composition can reveal the history of large-scale geologic processes.
38 Here we explore olivine spectra in the intermediate infrared region (IMIR), where systematic
39 trends in olivine's absorption bands are indicative of composition. We degrade laboratory olivine
40 spectra to data qualities that are more realistic of imaging spectrometers used in planetary
41 exploration and derive constraints on the signal-to-noise ratio and sampling rates required to
42 accurately prediction olivine composition. These constraints will be useful in the development of
43 IMIR imaging spectrometers.

44 **1 Introduction**

45 Olivine is an important rock forming mineral whose composition and early crystallization from
46 silicate melts make it useful for discerning distinct crustal terranes and understanding the origin
47 and evolution of magmatic sources. Geologically significant olivine-group minerals have
48 compositions falling on the Fe-Mg solid-solution series, varying in Mg# (molar $\text{Mg}/[\text{Mg}+\text{Fe}] * 100$)
49 between an Fe-rich endmember (fayalite, Mg# 0) and an Mg-rich endmember (forsterite,
50 Mg# 100), with high-Mg compositions indicative of more primitive primary magmas. For the
51 Moon and other planetary bodies, widespread characterization of olivine composition can
52 provide insight into the planet's bulk thermal and chemical evolution.

53
54 Spectral features of olivine are known to exhibit consistent trends with Mg# and have been used
55 to estimate olivine composition for certain locations on the Moon (e.g. Isaacson et al., 2011) and
56 globally on Mars (e.g. Koeppen & Hamilton, 2008). To date, remote determination of olivine
57 composition from spectroscopic data has been restricted to visible-near infrared (VNIR, 0.5 - 2

58 μm) and mid-infrared (MIR, 8 - 15 μm) wavelengths. In the VNIR, the position of three
59 overlapping 1 μm bands arising from electronic transitions of Fe^{2+} are diagnostic of Mg# (e.g.
60 Dyar et al., 2009) and can be inverted via the modified gaussian model (Sunshine et al., 1990) to
61 ascertain composition (e.g. Clénet et al., 2011). In the MIR, restrahten bands exhibit systematic
62 shifts in band strength and linear trends in band position with changing cation ratios (Hamilton
63 2009, Lane 2011).

64

65 More recently, Kremer et al., 2020 demonstrated that the position of olivine overtone-
66 combination bands at $\sim 5.6 \mu\text{m}$ and $\sim 6.0 \mu\text{m}$ exhibit systematic shifts to longer wavelengths with
67 increasing Mg#, establishing applications for the intermediate infrared region (IMIR, 4 - 8 μm)
68 in the remote determination of olivine composition. Additional advantages of IMIR spectroscopy
69 include the capacity for remote determination of pyroxene composition (Kremer et al., 2023), as
70 well as the presence of a 6.1 μm molecular water absorption and diminished effects from space
71 weathering (Kremer et al., 2022).

72

73 To date, the IMIR region has been underutilized in the characterization of planetary surfaces due
74 in part to previous engineering constraints that limited the viability of IMIR detectors as well as
75 an array of strong atmospheric absorptions that preclude obtaining spectral information from the
76 surface of bodies with non-negligible atmospheres. In addition, the IMIR region lies between the
77 well-studied visible-short wavelength infrared region that relies primarily on solar radiation and
78 the well studied mid-infrared wavelength region that relies primarily on emissivity. Currently the
79 only hyperspectral instruments that cover IMIR wavelengths are the James Webb Space
80 Telescope and the Stratospheric Observatory for Infrared Astronomy (SOFIA), an Earth-based
81 airborne telescopic observatory operating at stratospheric altitudes (Stutzki 2006) that has ceased
82 operations. SOFIA measurements of the lunar surface have been used to confirm the presence of
83 molecular water on the Moon via the detection of a 6.1 μm fundamental H_2O absorption
84 (Honniball et al., 2020), highlighting the potential of IMIR data in the surface characterization of
85 airless bodies. Recent advances in engineering have resulted in infrared detectors capable of
86 IMIR measurements (Ting et al., 2012, Cañas et al., 2020), positioning IMIR spectrometers as
87 valuable tools for lunar exploration.

88

89 The relationship between band position and olivine chemistry in the IMIR region was established
90 using laboratory data (Kremer et al., 2022), with spectral resolutions and signal-to-noise ratios
91 (SNR) exceeding those expected of imaging spectrometers. The SNR of data acquired onboard
92 spacecraft is known to decrease due to noise from electronic, optical, and thermal effects, and
93 instrument limitations restrict sampling rates when compared to laboratory measurements.
94 Variations in SNR and sampling rate may influence spectral interpretation by masking or
95 modifying absorption features at low SNRs or poorly resolving absorption features at lower
96 sampling rates (Swayze et al., 2003). In the case of remote determination of olivine composition
97 from IMIR datasets, SNR and sampling rates will influence both the detection and compositional
98 prediction of olivine.

99

100 Previous work that has studied the impact of data quality on spectral interpretation established
101 limits for mineral identification in the VNIR using spectra that had been convolved to the band-
102 passes and sampling intervals of various imaging spectrometers and further degraded with
103 random noise (Swayze et al., 2003). The authors used Tetracorder's feature fitting algorithm

104 (Clark et al., 2003) to determine best-fit matches between degraded input spectra and an
105 extensive spectral library that included a wide range of minerals and natural materials (Swayze et
106 al., 2003). The motivation behind employing a feature fitting algorithm was twofold; it takes
107 advantage of the full suite of spectral information within a given wavelength range and
108 normalizes first-order differences in band strength and background absorption for a given
109 spectral feature. This allows for direct comparison between spectra acquired under different
110 optical conditions and with varying sample characteristics. To determine the relationship
111 between band position and olivine composition in the IMIR region, Kremer et al. (2022)
112 measured the band minima position of the two strongest absorption features at $\sim 5.6 \mu\text{m}$ and ~ 6.0
113 μm . Additional features at $\sim 4.9 \mu\text{m}$, $\sim 5.2 \mu\text{m}$, and $\sim 5.4 \mu\text{m}$ attributed to olivine were not used
114 due to their weaker band strengths. In contrast, feature fitting makes use of the entire suite of
115 spectral features, analyzing all absorption bands simultaneously to understand the influence of
116 complete band shape on spectral interpretation.

117

118 Here we use a simplified feature fitting algorithm modeled after Tetracorder to determine the
119 effects of SNR and sampling interval on the identification and compositional determination of
120 olivine from IMIR spectra. Given the relevance of IMIR datasets to outstanding questions
121 regarding lunar exploration, we build our spectral library around a variety of lunar-relevant
122 minerals including a suite of synthetic olivine and pyroxene spectra of known compositions as
123 well as spectra of anorthite, spinel, and ilmenite. We analyze feature fitting results from
124 degraded spectra of olivine samples of known chemistry whose mineralogy and composition we
125 predict from feature fitting against library spectra. These samples, which we refer to as ‘test
126 spectra’ throughout, consist of 34 olivine samples of terrestrial, lunar, Martian, and synthetic
127 origin. Library and test spectra are described further in Section 2.1. We explore a range of data
128 qualities, degrading test spectra to SNRs of 50, 100, 150, 200, 300, 400, 500, and 600 and
129 sampling rates of 10 nm, 15 nm, 20 nm, 25 nm, 30 nm, 40 nm, 50 nm, and 60 nm. Methods for
130 noise superposition and downsampling are described in Section 2.2. Data quality constraints
131 required for accurate olivine detection and compositional prediction derived from this study will
132 feed forward into IMIR imaging spectrometer requirements.

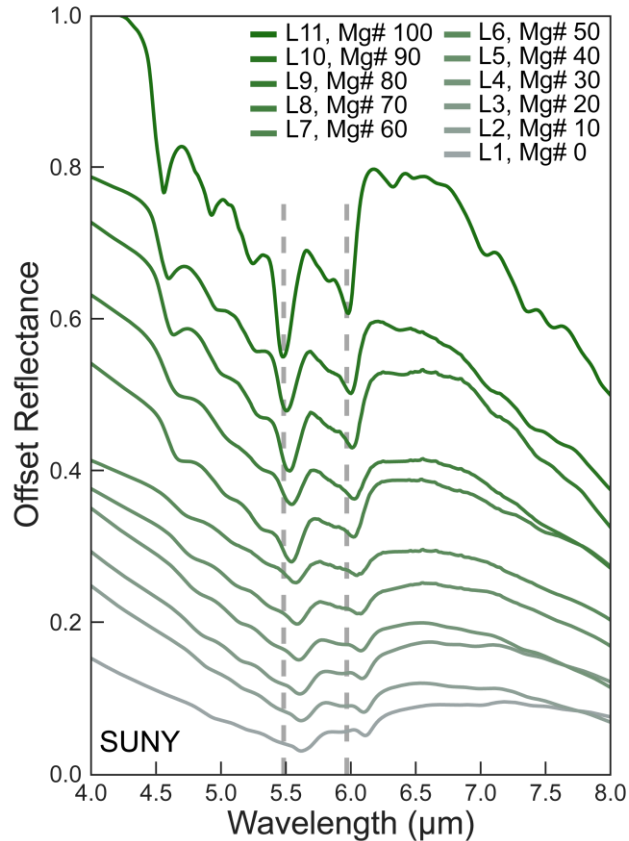
133 **2 Materials and Methods**

134 **2.1 Spectral Database**

135 Spectra used in this study were acquired from the PDS Geosciences Node Spectral Library and
136 the USGS Spectral Library. Spectra from the PDS Geosciences Node were measured at the
137 NASA Reflectance Experiment Laboratory (RELAB) at Brown University using a Thermo-
138 Nicolet Nexus 870 FTIR spectrometer (800 – 25,000 nm) and scaled to VNIR bidirectional
139 reflectance spectra (300-2600 nm). Spectra compiled from the USGS Spectral Library were
140 measured using either a Nicolet 740 FTIR or Magna-IR 762 FTIR and scaled to VNIR
141 reflectance spectra measured with a Beckman 5270 spectrometer.

142

143 Sample and measurement properties for all spectra used in this study are listed in Tables 1 & 2,
144 with spectra referred to by their sample # (TX for test spectra, LX for library spectra) or sample
145 name throughout the study.



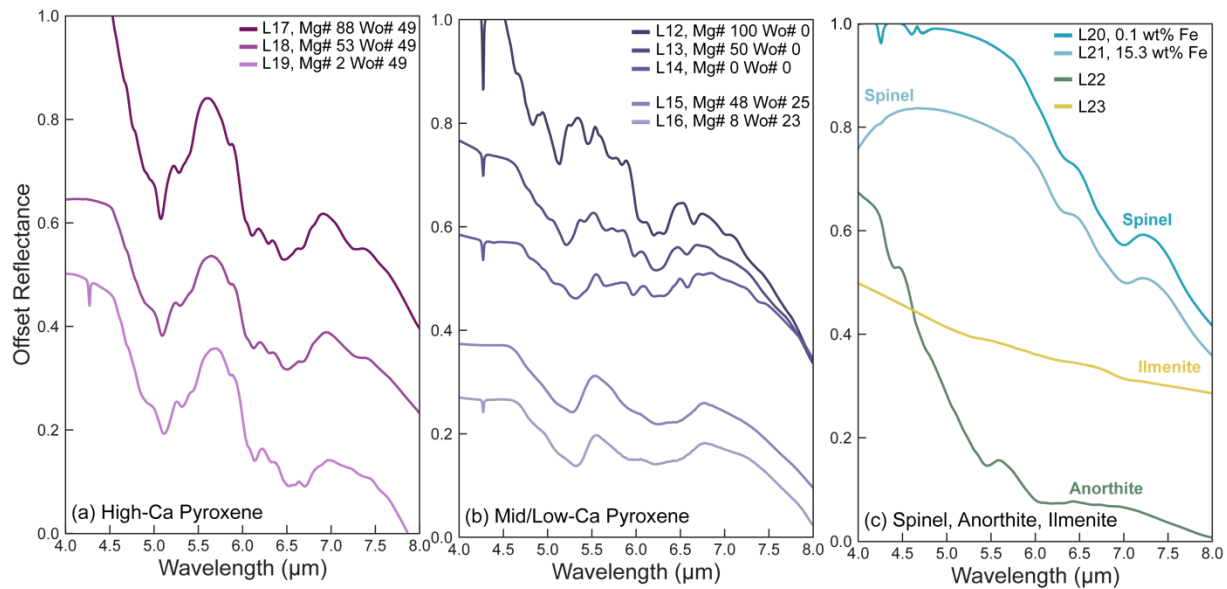
146
147 **Figure 1.** SUNY suite olivines. Note the trends in band position and muting of features with
148 decreasing Mg#.

149
150 **2.1.1 Library spectra**

151 Our spectral library is composed of reflectance data of synthetic olivine of varying composition
152 as well as a suite of lunar-relevant minerals including pyroxene, anorthite, spinel, and ilmenite.
153 We include 11 spectra of synthetic olivine (SUNY suite) synthesized by Donald Lindsley and
154 described in detail by Dyar et al., 2009. The suite consists of samples of high purity covering the
155 complete Mg-Fe solid solution series. We include spectra of synthetic olivine at approximately
156 10 Mg# intervals ranging from 0 to 100 and decide to forego inclusion of synthetic samples with
157 Mg#s 55, 65, and 75 to maintain a consistent interval between available library compositions
158 across the entire solid-solution series (Fig. 1, Table 1). The synthetic SUNY sample with a
159 composition between Mg# 80 and Mg# 100 falls slightly of the 10 Mg# interval with an Mg# of
160 89.5 instead of 90.

161
162 We also include a subset of spectra from a synthetic pyroxene suite synthesized by Donald
163 Lindsley (Fig. S1). The full suite consists of 43 samples covering a range of pyroxene
164 compositions spanning molar Ca content from 0 to 51 and Mg# from 0 to 100, and have been
165 used in previous infrared studies of pyroxene (e.g. Klima et al., 2010, Kremer et al., 2023). To
166 increase computational efficiency while still accounting for the influence of pyroxene
167 composition on spectral features in the IMIR region (Kremer et al., 2023), we chose to include
168 eight representative spectra from the larger 43-spectra dataset which covered endmember and

169 intermediate compositions across the pyroxene quadrilateral (Fig S1). Our spectral library also
 170 includes a spectrum of Miyake-jima anorthite with a Ca-composition (An# 98) comparable to
 171 that of the lunar anorthositic crust (e.g. Wood et al., 1970). We also provide endmember spectra
 172 (0.1 wt% FeO and 15.3 wt% FeO) from a suite of synthetic high-Mg spinel with lunar relevant
 173 compositions described in Jackson et al., 2014, as well as a spectrum of ilmenite separated from
 174 an Apollo 17 basalt. Library spectra are shown in Figs. 1 and 2 and sample characteristics and
 175 sources are listed in Table 1.
 176



177
 178 **Figure 2.** a) High-Ca synthetic pyroxenes covering the Mg-Fe solid-solution series. b) Mid and
 179 low-Ca synthetic pyroxenes covering the Mg-Fe solid solution series. c) Spinel, ilmenite, and
 180 anorthite. All spectra were acquired from RELAB and are described in Table 1.
 181
 182
 183

Table 1. Library Spectra

Sample #	Mineral	Origin	Composition	Particle size (μm)	Native Sampling Rate	Sample Identifier (Source)
L1	Olivine	Synthetic (SUNY)	Mg# 0	<45	3 nm – 12 nm	DD-MDD-098 (RELAB)
L2	Olivine	Synthetic (SUNY)	Mg# 10	<45	3 nm – 12 nm	DD-MDD-097 (RELAB)
L3	Olivine	Synthetic (SUNY)	Mg# 20	<45	3 nm – 12 nm	DD-MDD-096 (RELAB)
L4	Olivine	Synthetic (SUNY)	Mg# 30	<45	3 nm – 12 nm	DD-MDD-095 (RELAB)
L5	Olivine	Synthetic (SUNY)	Mg# 40	<45	3 nm – 12 nm	DD-MDD-094 (RELAB)
L6	Olivine	Synthetic (SUNY)	Mg# 50	<45	3 nm – 12 nm	DD-MDD-093 (RELAB)
L7	Olivine	Synthetic (SUNY)	Mg# 60	<45	3 nm – 12 nm	DD-MDD-091 (RELAB)
L8	Olivine	Synthetic (SUNY)	Mg# 70	<45	3 nm – 12 nm	DD-MDD-089 (RELAB)

L9	Olivine	Synthetic (SUNY)	Mg# 80	<45	3 nm – 12 nm	DD-MDD-087 (RELAB)
L10	Olivine	Synthetic (SUNY)	Mg# 89.5	<45	3 nm – 12 nm	DD-MDD-086 (RELAB)
L11	Olivine	Synthetic (SUNY)	Mg# 100	<45	3 nm – 12 nm	DD-MDD-085 (RELAB)
L12	Pyroxene	Synthetic	Mg# 100 Wo 0	<45	3 nm – 12 nm	DL-CMP-001 (RELAB)
L13	Pyroxene	Synthetic	Mg# 50 Wo 0	<45	3 nm – 12 nm	DL-CMP-004 (RELAB)
L14	Pyroxene	Synthetic	Mg# 0 Wo 0	<45	3 nm – 12 nm	DL-CMP-061 (RELAB)
L15	Pyroxene	Synthetic	Mg# 48 Wo 25	<45	3 nm – 12 nm	DL-CMP-057 (RELAB)
L16	Pyroxene	Synthetic	Mg# 8 Wo 2 3	<45	3 nm – 12 nm	DL-CMP-054 (RELAB)
L17	Pyroxene	Synthetic	Mg# 88 Wo 49	<45	3 nm – 12 nm	DL-CMP-043 (RELAB)
L18	Pyroxene	Synthetic	Mg# 53 Wo 49	<45	3 nm – 12 nm	DL-CMP-036 (RELAB)
L19	Pyroxene	Synthetic	Mg# 2 Wo 49	<45	3 nm – 12 nm	DL-CMP-082 (RELAB)
L20	Spinel	Synthetic	0.1 wt% FeO	<45	3 nm – 12 nm	SP-CMP-073-B (RELAB)
L21	Spinel	Synthetic	15.3 wt% FeO	<45	3 nm – 12 nm	SP-CMP-083-B (RELAB)
L22	Plagioclase	Miyake-jima	An# 98	45-75	3 nm – 12 nm	PL-CMP-151-C (RELAB)
L23	Ilmenite	Apollo 17	--	<45	3 nm – 12 nm	LR-CMP-222 (RELAB)

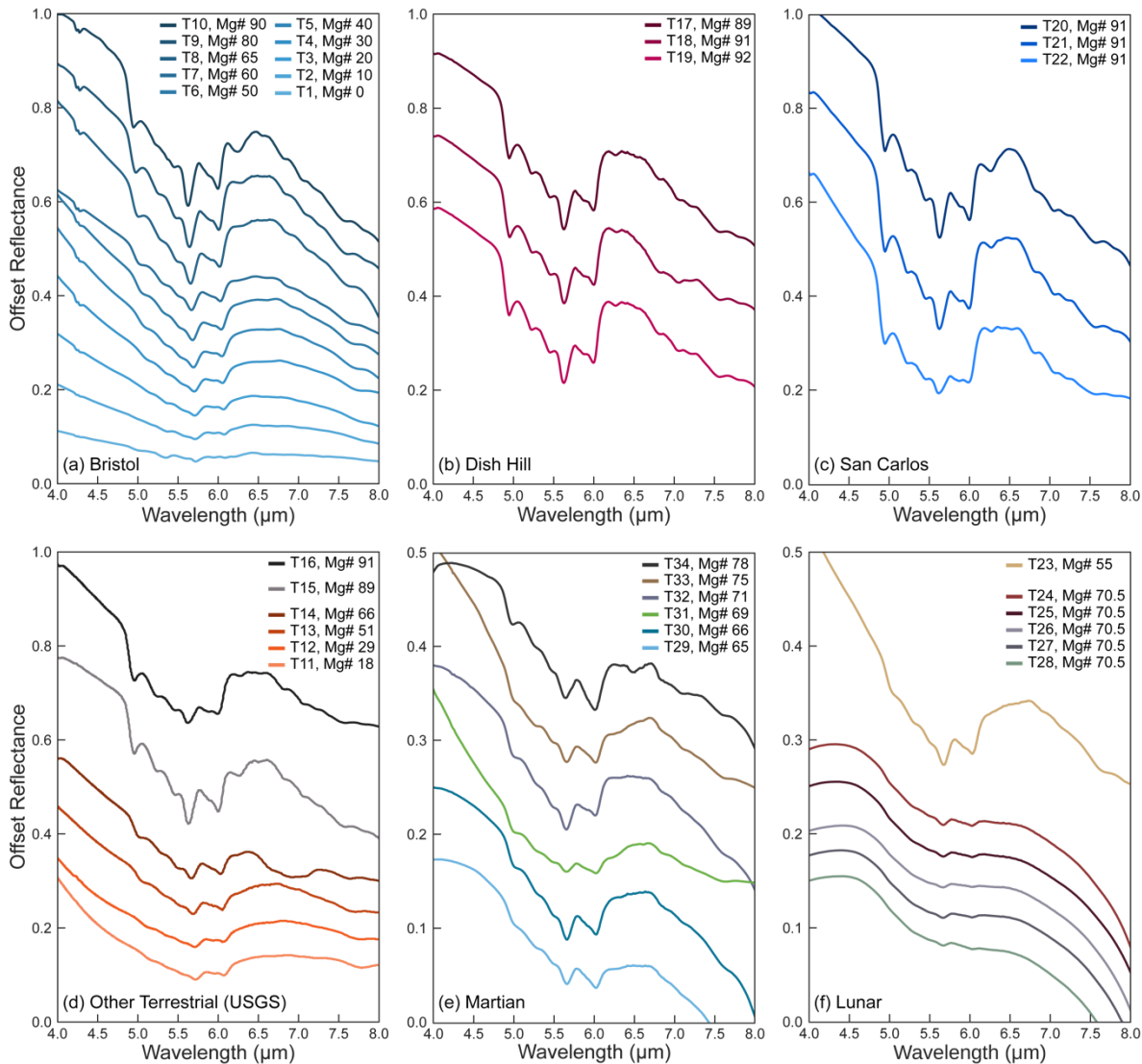
184

185 **2.1.2 Test spectra**

186 Test spectra consisted of reflectance data measured from a diverse range of synthetic, terrestrial,
 187 and extraterrestrial olivine with known compositions. These spectra were previously used to
 188 establish the relationship between band position and olivine chemistry in the IMIR region by
 189 Kremer et al., 2020. With the exception of the Apollo 74002 drive tube (T24-28), all test spectra
 190 were measured as particulate samples and consisted of pure olivine.

191

192 We include a second suite of synthetic olivine spectra (Bristol suite) which were synthesized by
 193 Richard Brooker and are described in Dyar et al., 2009 (Fig. 3a). We chose the SUNY suite as
 194 library spectra and the Bristol suite as test spectra based on the SUNY suite's greater chemical
 195 purity and comprehensive coverage of Mg# values at regular intervals. The Bristol suite, by
 196 contrast, had minor contamination of up to 18.7% Fe³⁺ and Mg# values ranging from 0 to 90
 197 (Darby et al., 2009). Test spectra of terrestrial samples included olivine specimens from Dish
 198 Hill, California (Fig. 3b) and San Carlos, Arizona (Fig. 3c), as well as samples from the
 199 Kiglapait intrusion in Labrador, South Point, Hawaii, and Twin Sister Peak, Washington (Fig.
 200 3d). Spectra of extraterrestrial samples included Martian meteorites Yamato 984028, Chassigny,
 201 NWA 2737, ALH 77005, and EETA 79001 (Fig. 3e). Lunar samples (Fig. 3f) included olivine
 202 extracted from a mare basalt (Apollo return sample 15555) as well as five spectra from different
 203 depths of the Apollo 74002 drive tube, a sample composed of ilmenite-rich pyroclastic beads
 204 hosting microscopic inclusions of olivine (Heiken & McKay, 1978).



205
 206 **Figure 3.** Test spectra included in this study. a) Synthetic Bristol suite. b) Dish Hill, California.
 207 c) San Carlos, Arizona. d) Twin Sister Peak, WA, South Point, HI, and Kiglapait intrusion. e)
 208 Martian meteorite samples NWA2737, EETA79001, ALH77005, Chassigny, Yamato-984028. f)
 209 Lunar samples 15555 separate and drive tube 74002. With the exception of the spectra in panel d
 210 which were acquired from the USGS spectral library, all spectra were acquired from RELAB and
 211 are described in Table 2.

212
 213

Table 2. Test Spectra

Sample #	Sample Name	Origin	True Mg#	Predicted Mg#*	Particle size (μm)	Sampling Rate (nm)	Sample Identifier (Source)	IBD
T1	Bristol-046	Synthetic (Bristol)	0	20	<45	3 - 12	DD-MDD-046 (RELAB)	0.099
T2	Bristol-045	Synthetic (Bristol)	10	20	<45	3 - 12	DD-MDD-045 (RELAB)	0.101
T3	Bristol-044	Synthetic (Bristol)	20	20	<45	3 - 12	DD-MDD-044	0.113

							(RELAB)	
T4	Bristol-043	Synthetic (Bristol)	30	30	<45	3 - 12	DD-MDD-043 (RELAB)	0.146
T5	Bristol-042	Synthetic (Bristol)	40	30	<45	3 - 12	DD-MDD-042 (RELAB)	0.165
T6	Bristol-041	Synthetic (Bristol)	50	50	<45	3 - 12	DD-MDD-041 (RELAB)	0.161
T7	Bristol-040	Synthetic (Bristol)	60	70	<45	3 - 12	DD-MDD-040 (RELAB)	0.142
T8	Bristol-039	Synthetic (Bristol)	65	70	<45	3 - 12	DD-MDD-039 (RELAB)	0.181
T9	Bristol-038	Synthetic (Bristol)	80	80	<45	3 - 12	DD-MDD-038 (RELAB)	0.188
T10	Bristol-037	Synthetic (Bristol)	90	89.5	<45	3 - 12	DD-MDD-037 (RELAB)	0.202
T11	KI3377	Kiglapait	18	10	<60	10	KI3377 (USGS)	0.222
T12	KI3291	Kiglapait	29	10	<60	10	KI3291 (USGS)	0.213
T13	KI3188	Kiglapait	51	40	<60	10	KI3188 (USGS)	0.201
T14	KI3054	Kiglapait	66	60	<60	10	KI3054 (USGS)	0.190
T15	GDS70.d	South Point, HI	89	80	<60	10	GDS70.d (USGS)	0.226
T16	GDS71.b	Twin Sisters Peak, WA	91	89.5	<60	10	GDS71.b (USGS)	0.393
T17	DishHill-078	Dish Hill, CA	89	89.5	<45	3 - 12	DD-MDD-078 (RELAB)	0.226
T18	DishHill-076	Dish Hill, CA	91	89.5	<45	3 - 12	DD-MDD-076 (RELAB)	0.205
T19	DishHill-077	Dish Hill, CA	92	89.5	<45	3 - 12	DD-MDD-077 (RELAB)	0.201
T20	SanCarlos-080A	San Carlos, AZ	91	80	<63	3 - 12	PO-CMP- 080A (RELAB)	0.247
T21	SanCarlos-080B	San Carlos, AZ	91	89.5	63-125	3 - 12	PO-CMP- 080B (RELAB)	0.283
T22	SanCarlos-080C	San Carlos, AZ	91	100	125-250	3 - 12	PO-CMP- 080C (RELAB)	0.415
T23	15555 Separate	Moon	55	70	<45	3 - 12	LR-CMP-212 (RELAB)	0.099
T24	74002.332	Moon	70.5	70	<500	3 - 12	LR-CMP-130 (RELAB)	0.063
T25	74002.2216	Moon	70.5	60	<501	3 - 12	LR-CMP-131 (RELAB)	0.072
T26	74002.2217	Moon	70.5	60	<502	3 - 12	LR-CMP-132 (RELAB)	0.065
T27	74002.2218	Moon	70.5	60	<503	3 - 12	LR-CMP-133 (RELAB)	0.081
T28	74002.2219	Moon	70.5	70	<504	3 - 12	LR-CMP-134 (RELAB)	0.084
T29	Y-984028-I	Mars	65	70	<45	3 - 12	DD-MDD-121	0.108

							(RELAB)	
T30	Y-984028-E	Mars	66	70	<45	3 - 12	DD-MDD-122 (RELAB)	0.138
T31	Chassigny	Mars	69	70	<50	3 - 12	DD-MDD-001 (RELAB)	0.343
T32	ALH77005	Mars	71	60	<50	3 - 12	DD-MDD-009 (RELAB)	0.166
T33	EETA79001	Mars	75	70	<50	3 - 12	DD-MDD-060 (RELAB)	0.268
T34	NWA2737	Mars	78	70	<45	3 - 12	DD-AHT-065 (RELAB)	0.170

214 *Mg# predicted from feature fitting on laboratory-quality data

215

216 **2.2 Spectral Degradation:**

217 We explore the influence of noise and spectral resolution on spectral interpretation by degrading
 218 test spectra to a range of SNRs and sampling rates. For a given round of feature fitting, the test
 219 spectrum and library spectra were resampled to a given sampling rate (Section 2.2.1) and further
 220 degraded with the superposition of noise (Section 2.2.2). Degraded test spectra were then
 221 subjected to a feature fitting algorithm and compared against library spectra (Section 2.3), with
 222 best-fit library matches recorded and used to evaluate the impact of noise and sampling on
 223 spectral interpretation.

224

225 **2.2.1 Resampling**

226 To explore the effect of sampling rate on spectral interpretation, Swayze et al., 2003 used band
 227 pass and sampling interval information from four imaging spectrometers (AVIRIS, HYDICE,
 228 MIVIS, and VIMS) to reproduce the spectrometer's spectral resolution. Here we focus on a
 229 simple downsampling of the laboratory data by calculating resampled reflectance values as a
 230 weighted sum of the fraction of reflectance values in the original wavelength domain that fall
 231 under the resampled wavelength domain. We resample test spectra before the superposition of
 232 noise.

233

234 We limit our resampling to uniform sampling intervals beginning at 4 μm and resample spectra
 235 to intervals of 10 nm, 15 nm, 20 nm, 25 nm, 30 nm, 40 nm, 50 nm, and 60 nm. Sampling rates
 236 for laboratory spectra acquired from the USGS and RELAB databases were 10 nm and 3 nm –
 237 12 nm across IMIR wavelengths, respectively.

238

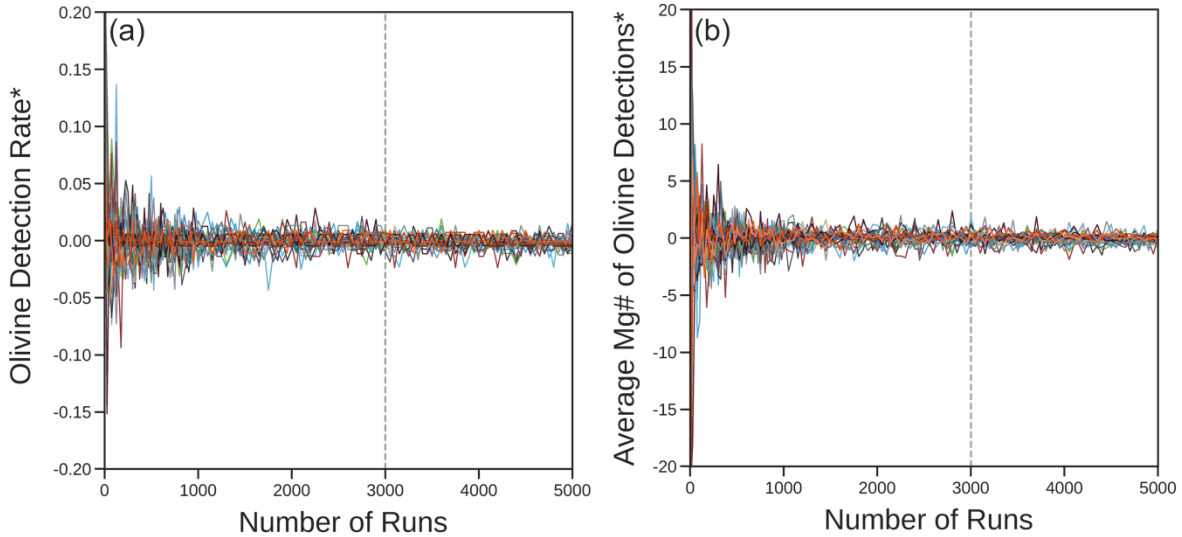
239 **2.2.2 Noise**

240 Increasing levels of scaled gaussian noise were superimposed on test spectra uniformly across all
 241 wavelengths. Noise spectra were randomly sampled from a normal distribution with a mean of
 242 zero and a set standard deviation. Following Swayze et al., 2003, we define SNR for a surface of
 243 50% reflectance, where a reflectance level of 0.5 is divided by the standard deviation of the noise
 244 spectrum.

245

246 Each noise spectrum defined by an SNR represents a random draw from the given distribution,
 247 with individual outcomes varying. To ensure statistical precision for each round of feature fitting
 248 we downsampled and degraded all test spectra to the lowest data qualities explored in this study
 249 (SNR 50, sampling rate 60 nm) and calculated the variance in olivine detection rates and average
 250 Mg# prediction across an increasing number of runs. After ~1500 runs, variations in olivine

251 detection rates were well within $\pm 2.5\%$ and variations in average Mg# prediction were well
 252 within ± 2.5 Mg#, with minimal increases in precision observed over a greater number of runs
 253 (Fig. 4). For each round of feature fitting we degrade test spectra to a given sampling rate and
 254 SNR for 3000 rounds. For each iteration, the test spectrum is degraded via the superposition of a
 255 new noise spectrum which is randomly sampled from the gaussian distribution defined by that
 256 round's SNR.

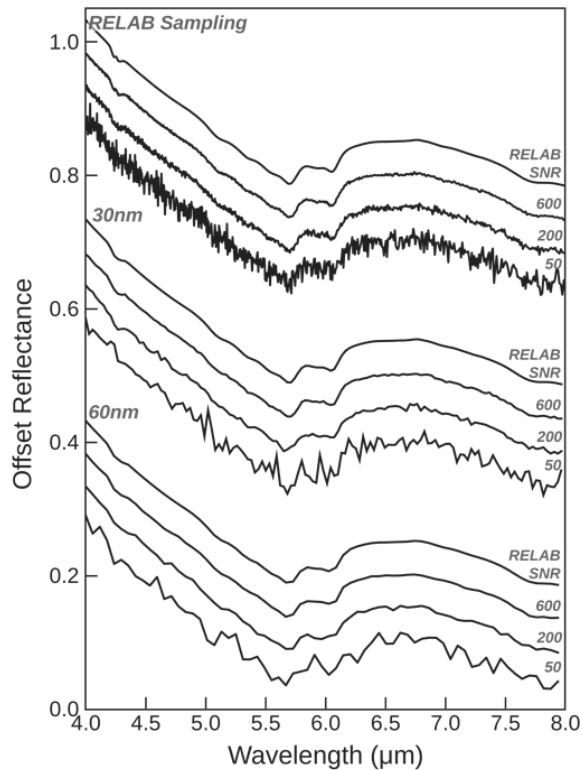


257 **Figure. 4** a) Olivine detection rate and b) average Mg# of olivine detections for all test spectra across an increasing
 258 number of runs. *Data has been demeaned for clarity. Raw data is shown in Fig. S2.
 259

260
 261 We degrade spectra to SNRs of 50, 100, 150, 200, 300, 400, 500, and 600. Our choice to define
 262 SNR relative to a surface of 50% reflectance allows us to standardize discussion of SNR
 263 throughout the work, however equivalent SNRs will have different relative effects on test spectra
 264 depending on the samples spectral contrast. To place SNR in context with the test spectrum's
 265 spectral contrast, we calculate integrated band depths (IBDs) following Milliken & Mustard,
 266 2005 (eq. 1), where $R(\lambda)$ represents the reflectance value of the absorption, $R_c(\lambda)$ represents the
 267 reflectance value of the continuum, and $d\lambda$ is the sampling interval. IBD values serve as an
 268 approximation of the cumulative energy represented by all absorptions occurring within the
 269 integrated spectral range (Milliken & Mustard, 2005). For uniformity, all test spectra were
 270 resampled to 10 nm for the IBD calculations listed in Table 2.
 271

$$272 \quad IBD = \frac{\int_{\lambda_{min}}^{\lambda_{max}} 1 - \frac{R(\lambda)}{R_c(\lambda)} d\lambda}{\lambda_{max} - \lambda_{min}} \quad (1)$$

273
 274 An example of degraded test spectra across the range of SNRs and sampling rates explored in
 275 this study are shown in Fig. 5.



276
 277 **Figure 5.** Bristol Mg# 30 spectra degraded to various combination of SNR and sampling rate
 278 explored in this study. RELAB sampling rates range from 3 nm – 12 nm across IMIR
 279 wavelengths.

280
 281

282 **2.3 Feature Fitting:**

283 We calculate best-fit matches between artificially degraded olivine spectra of known
 284 composition and a spectral library of lunar-relevant minerals as described in Section 2.1.1. Test
 285 spectra consisted of synthetic and natural olivine samples as described in Section 2.1.2.
 286

287 For a single round of feature fitting, we start by isolating the spectral feature of interest by
 288 removing a continuum defined by the spectra's convex-hull (Fig. 6b). The feature fitting routine
 289 requires that a continuum be removed using a set of fixed channels bounding the feature of
 290 interest. We determine band positions for the continuum boundaries from the convex hull of the
 291 SUNY Mg#100 library spectrum since high-Mg olivine endmembers exhibit the strongest
 292 spectral features in this wavelength range. The resulting continuum bounds were found to be
 293 4.69 μm and 6.56 μm on the original wavelength domain. In rounds where spectra were
 294 resampled, the bands closest to those values were selected.
 295

296 In the IMIR region, smaller particle sizes result in greater spectral contrast (e.g. Fig. 3c, T20-
 297 T22). We account for the first order effects of grain size and band saturation via a linear gain and
 298 offset measurement (Clark et al., 2003). The linear gain and offset adjustment serves to
 299 normalize spectral contrast between the test spectrum and library spectra and its simplicity

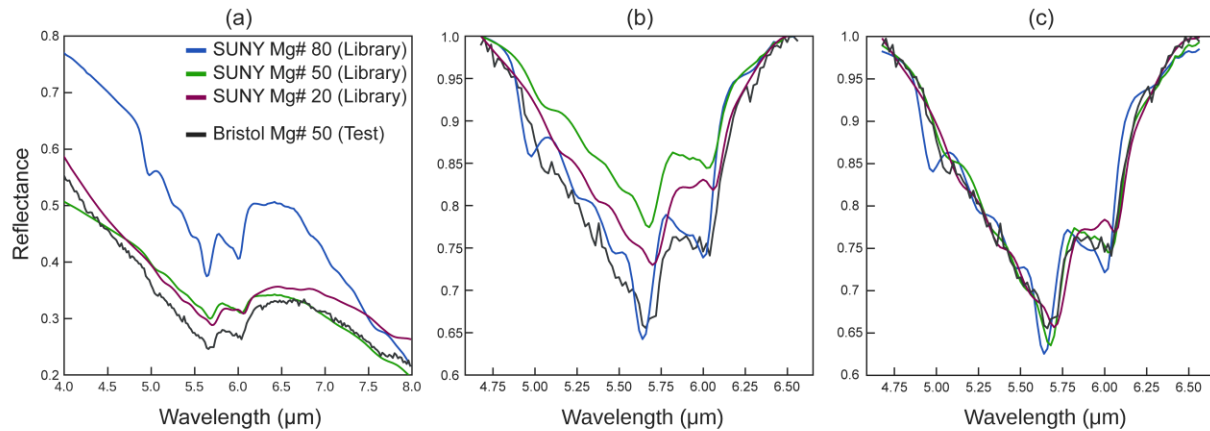
300 enables rapid digestion of large spectral datasets (Fig. 6c). An adjusted library spectrum is
 301 calculated by using an additive constant, k
 302

$$R'(\lambda) = \frac{R_{CR}(\lambda) + k}{1.0 + k} \quad (2)$$

303 where R_{CR} represents the continuum-removed library reflectance values. The linear form of eq. 2
 304 can be written as follows:
 305
 306

$$R' = \frac{k}{1.0 + k} + \frac{1.0}{1.0 + k} R_{CR} \quad (3)$$

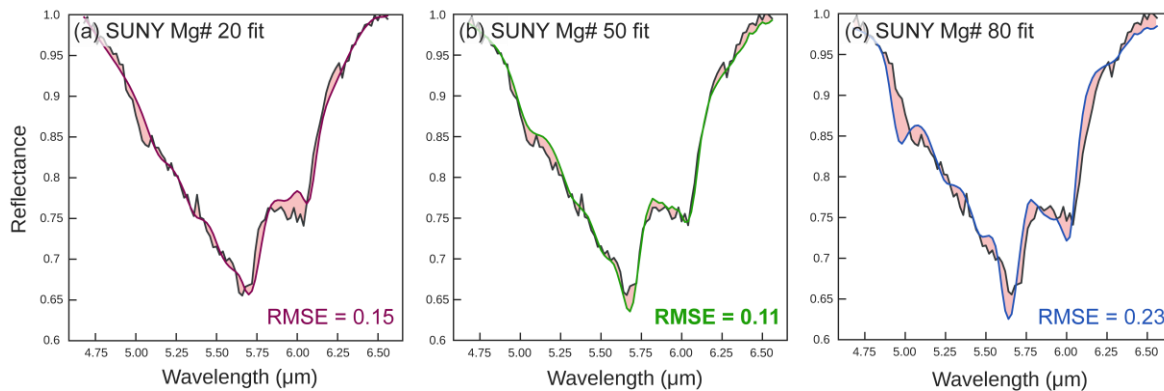
307 A standard linear least-squares regression is then used to determine the optimal k value to fit the
 308 adjusted library spectrum to the degraded test spectrum.
 309
 310



311
 312 **Figure 6.** Simplified example of a feature fitting routine with degraded Bristol-041 spectrum
 313 (200 SNR, 20 nm sampling) and three library spectra, SUNY Mg# 20, 50, and 80. a) Laboratory
 314 reflectance data of degraded test and library samples. b) Continuum-removed reflectance. c)
 315 Library spectra fit to degraded Bristol spectra following a linear-gain and offset adjustment.

316 The library spectrum that provides the best overall fit is determined by calculating the Root
 317 Mean Square Error (RMSE) between the continuum-removed test spectrum and each optimized
 318 library spectra (Fig. 7). Each round serves as a unique spectral interpretation with the best-fit
 319 library spectra taken as a mineral detection. We refrain from specifying an RMSE threshold
 320 required for identification since there was no value that would serve to minimize the number of
 321 false detections while not concurrently negating a large number of true detections. In this regard,
 322 this study serves to identify upper limits on SNRs and sampling rates required for olivine
 323 detection and accurate interpretation of olivine chemistry from IMIR data.
 324
 325

326 Because the composition of all the olivine samples included as both test and library spectra are
 327 known, in rounds where olivine was detected the composition of the best-fit library spectra was
 328 further considered as an Mg# prediction for the degraded test spectra (Fig. 7). Identification rates
 329 were then calculated for test spectra degraded to various data qualities.



330
 331 **Figure. 7** RMSE calculation of three library spectra after feature fitting a) SUNY Mg#20, b)
 332 SUNY Mg# 50, c) SUNY Mg# 80. Here, SUNY Mg#50 had the lowest RMSE and is considered
 333 the best-fit mineral and subsequent Mg# prediction for the degraded Bristol-048 spectrum whose
 334 true Mg# is 50.

335 3 Results

336 3.1 Olivine Identification Rates

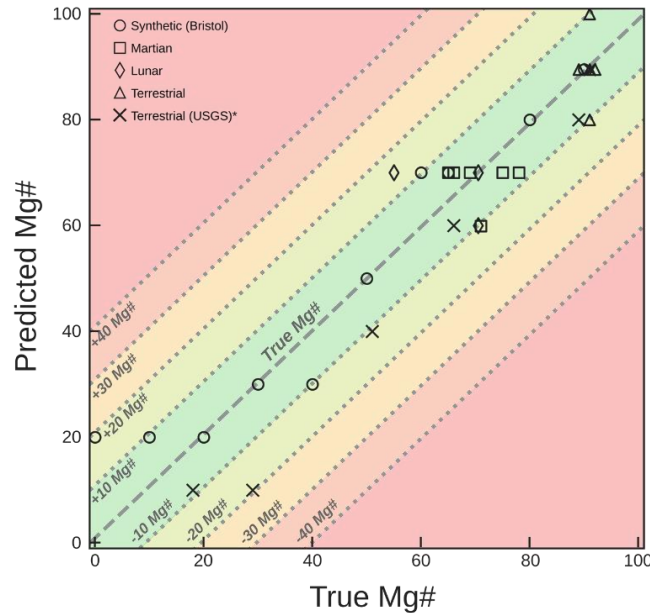
337 For each round of feature fitting we consider the best-fit library spectra as a mineral detection
 338 regardless of composition. For all test spectra degraded to any combination of SNR and sampling
 339 rate, olivine was the predominant mineral detection across a set of feature fitting runs. The
 340 parameter space required to achieve 100% olivine detection across all test spectra are shown in
 341 Fig. S3.

342
 343 With the exception of Chassigny, test spectra with high spectral contrast were correctly identified
 344 as olivine over all feature fitting runs across all combinations of SNR and sampling rates
 345 explored (Fig. S3). Notably, the Chassigny test spectrum, which had a relatively large IBD of
 346 0.343, was falsely identified as anorthite up to 15% of the time when degraded to the lowest data
 347 qualities. While olivine detections dominated regardless of test spectrum or data quality, for
 348 samples with lower IBDs (e.g. low-Mg synthetic samples (T1-2), lunar samples (T23-28), and
 349 sample Y-984928-I (T29)), test spectra degraded to low-SNRs and high-sampling rates would
 350 occasionally be falsely-identified as ilmenite or anorthite, with minimal false detections of spinel
 351 or pyroxene. Across the over 6.5 million feature fitting runs covering all SNRs, sampling rates,
 352 and test spectra explored here, pyroxene was falsely detected only 540 times. False detections of
 353 ilmenite and anorthite were confined to SNRs ≤ 150 and accounted for only 0.30% and 0.20% of
 354 all detections, respectively.

355
 356 The sample that required the finest data qualities (highest SNRs and finest sampling rates) to
 357 reach 100% olivine detection was the Apollo drive tube sample 74002.332 (T24 – 28). In order
 358 to achieve 100% olivine detection for this sample, spectra had to have an SNR of 100 for a
 359 sampling rate of 10 nm, SNRs ≥ 150 for sampling rates under 30 nm, and SNRs ≥ 200 for
 360 sampling rates of 40 - 60 nm.

361 3.2 Compositional Prediction of Olivine Using Feature Fitting on Laboratory-Quality Data

363 We first investigate the accuracy of our feature fitting routine on compositional determination of
 364 laboratory-quality data. Across the 34 test spectra, the average absolute error in Mg# prediction
 365 was 6.39 mol%, reinforcing the utility of IMIR wavelengths in the determination of olivine
 366 composition as well as the application of our feature fitting routine for compositional prediction.
 367 35% of test spectra (12 out of 34 samples) were predicted within ± 2 Mg# of their true
 368 compositions, 91% of test spectra (31 out of 34 samples) were predicted to be within ± 11 Mg#
 369 of their true compositions, and the remaining three test spectra were predicted to be within ± 20
 370 Mg# of their true compositions (Fig. 8).
 371



372
 373 **Figure 8.** Undegraded test spectra true Mg# plotted against Mg# prediction from feature fitting.
 374 *For USGS samples, all spectra were resampled to 10 nm since test spectra and library spectra
 375 had different native sampling domains.

376

377 3.3 Effects of SNR and Sampling Rate on Olivine Mg# Interpretation

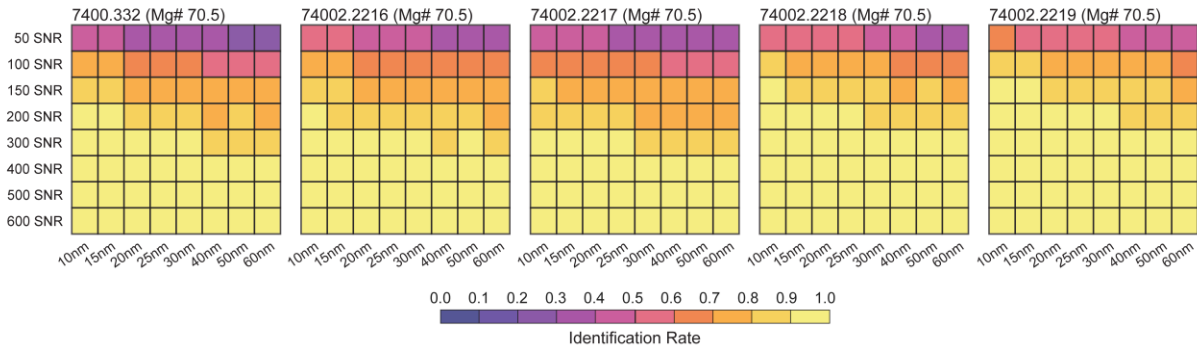
378 We then study the effects of spectral degradation on compositional interpretation for the 31 test
 379 spectra predicted within ± 11 Mg# of their true composition on laboratory quality data. We
 380 forego analysis of Bristol-046 (T1), KI3291 (T12), and the 15555 Separate (T23) since their
 381 compositional predictions fell outside of this range (Section 3.2).

382

383 Significant variations in the accuracy of compositional predictions were observed among test
 384 spectra that had been degraded to a given SNR and sampling rate. The Dish Hill (T17 -19), San
 385 Carlos (T20 – 22), Bristol-038 (T9), GDS71.b (T16) samples, all of which displayed well-
 386 defined absorptions with high IBDs, were predicted within ± 11 Mg# of their true composition
 387 across all runs for the data qualities explored here (Fig. S4). Nine other samples (T5, T7, T8,
 388 T13, T14, T20, T32, T33) were predicted within ± 11 Mg# of their true composition for $\geq 90\%$
 389 runs for SNRs ≥ 50 . The lunar drive tube samples (T24 – 28) required SNRs greater than 200 to
 390 achieve $\geq 90\%$ compositional prediction within ± 11 Mg# for the sampling intervals explored
 391 here (Fig. 9).

392
393
394
395
396
397
398
399
400

The only test spectrum that did not reach $\geq 90\%$ compositional prediction within ± 11 Mg# across the parameter space explored here was Y-984028-E (T30), which has an Mg# of 66 and was predicted as Mg# 70 on laboratory quality data using the feature fitting routine. At high SNRs (≥ 400) and low sampling rates (≤ 20 nm), best-fit predictions for Y-984028-E oscillated between Mg# 70 and Mg# 50. At the least-degraded data quality (SNR 600 and sampling rate of 10 nm), $\sim 76\%$ of best-fit library matches were Mg# 70 (4 mol% from true value), while the remaining detections interpreted the composition as Mg# 50 (16 mol% from true value).



401
402
403
404

Figure. 9 Identification rates within ± 11 Mg# of test spectrum's true composition. Each grid space represents the result of 3000 feature fits, with each iteration generating a new degraded test spectra from randomly sampled noise defined by that grid's SNR and resampled to the grid's sampling rate.

405 4 Discussion

406 4.1 Olivine Detection in the IMIR Region

407 In the VNIR, olivine interpretation is complicated both by the fact that olivine has 3 overlapping
408 features at 1 μm and by the fact that the 3-band composite feature overlaps with a broad 0.9 μm
409 pyroxene absorption arising from electronic transitions. In contrast, in the IMIR region, olivine
410 absorptions are the result of multiple, discrete overtone-combination bands (Kremer et al., 2020).
411 The spectral complexity results in readily distinguishable spectral signatures for olivine when
412 compared to pyroxene and other lunar-relevant minerals across IMIR wavelengths (e.g. Figs. 1 &
413 2). For the test spectra explored here, olivine was by far the most common best-fit library
414 mineral for a given set of feature fitting runs when compared to pyroxene, anorthite, spinel, and
415 ilmenite.

416

417 4.2 Successful Compositional Prediction via Feature Fitting

418 The low absolute error in Mg# prediction across laboratory-quality data strengthens the validity
419 of utilizing IMIR wavelengths for remote determination of olivine composition and emphasizes
420 the practicality of employing a feature fitting approach for predictive compositional analysis.

421

422 The synthetic olivine suite included in our spectral library was limited to samples covering the
423 solid-solution series at intervals of roughly 10 Mg#. Prediction accuracy for a given round of
424 feature fitting is constrained by the available olivine compositions in the spectral library (e.g. a
425 test spectra of known Mg# 65 could at best be predicted with an error of 5 mol%, as either Mg#
426 60 or Mg# 70). Accuracy of the feature fitting routine is thus directly tied to the spectral library,
427 and can be improved upon with synthetic suites that cover the solid-solution series at finer

428 intervals, or expanded upon for other applications, for example with library spectra of lunar-
429 relevant mixtures. This is in contrast to the band-minima technique employed by Kremer et al.,
430 2020, where the prediction accuracy is limited instead by spectral resolution and can be strongly
431 effected by SNR. For a sampling rate of just 20 nm, the resolution in Mg# prediction using the
432 band minima equations derived by Kremer et al., 2020 would be ~ 17 Mg# for the 5.6 μm band
433 and ~ 19 Mg# for the 6 μm band.

434 **4.3 Effects of Degradation on Compositional Prediction**

435 Mineral detection requires sufficient spectral contrast to detect absorption features diagnostic of
436 a mineral's crystal structure. With regards to remote determination of olivine Mg# from
437 degraded IMIR spectra, spectral contrast will influence the degradation thresholds required for
438 accurate mineral detection as well as any subsequent compositional predictions. Since we define
439 our SNR relative to a surface of 50% reflectance, test spectra with smaller IBDs generally
440 required higher SNRs before reaching a given identification threshold.

441 **4.3.1 Insights From Synthetic Samples**

442 The Bristol suite highlights a general trend in both increasing olivine detection rates and
443 increasing accuracy of compositional interpretation with increasing Mg#. In the IMIR region,
444 absorption strengths increase with magnesium concentration. Consequently, targets with higher
445 Mg# exhibit increased spectral contrast, making them favorable for detection and compositional
446 analysis. This carries significant implications for the exploration of Mercury, whose surface
447 lacks significant amounts of ferrous iron resulting in an absence of detectable spectral features in
448 VNIR data (McCord & Clark 1979, Nittler et al., 2011). The Mg# of returned lunar samples has
449 been relatively high, with ferroan anorthosites and alkali-suite samples falling in the range of
450 ~ 30 to ~ 70 Mg# and Mg-suite samples having Mg#s greater than ~ 60 (Shearer et al., 2015).

451 **4.3.2 Insights From Natural Samples**

452 The variability in identification rates across terrestrial, Martian, and lunar test spectra reveals the
453 numerous factors that play a role in spectral interpretation when examining natural samples.
454 Band strengths and band shapes will vary with olivine composition, grain size, and mineral
455 abundance in mixtures. Spectral shape and spectral contrast will further be influenced by the
456 presence of alteration products, chemical impurities and minor cation substitutions, and, for lunar
457 samples, space weathering effects.

458 A strength of the band-minima approach employed by Kremer et al., 2020 is that compositional
459 prediction relies solely on the band minima position of the ~ 5.6 μm and ~ 6.0 μm bands and is
460 therefore less impacted by overall band shape. While the feature fitting routine normalizes first-
461 order differences in band strength via a linear scaling routine, the various physical and chemical
462 parameters affecting band strength will also influence the overall spectral shape and subsequent
463 mineralogic and compositional interpretations.

464 An example can be seen in the three San Carlos samples (T20 – T22), which were identical in
465 composition (Mg #91) and sample characteristics besides grain size. Reflectance measurements
466 are highly grain size dependent as grain size dictates the internal path length traveled by photons
467 and the proportions of the photons that are absorbed versus scattered (Clark & Roush 1984,
468 Clark 1999). The three San Carlos samples were estimated to have Mg#s of 80, 89.5 and 100 on

474 undegraded data using the feature fitting routine for grain sizes of $<63 \mu\text{m}$, $63 - 125 \mu\text{m}$, and 125
475 $- 250 \mu\text{m}$, respectively. While all three estimations, regardless of grain size, fell within $\pm 11 \text{ Mg\#}$
476 of the sample's true composition, it demonstrates how feature fitting accuracy is dependent on all
477 factors controlling the overall spectral shape, of which composition is only one.

478

479 **4.3.3 Olivine Separates and Bulk Measurements**

480

481 Of the 34 test spectra used in this study, 30 were olivine samples which had been separated from
482 their original matrix. In the context of planetary exploration, a given pixel measured by an
483 imaging spectrometer will almost certainly represent a mixture of materials in contact as either
484 regolith or rock. The resulting spectra will be a non-linear combination of the end-member
485 components of the mixture, which will affect the overall band shape and may influence
486 compositional predictions via the feature fitting routine. Four test spectra acquired from the
487 Apollo 74002 drive tube (T25-28) were measured as bulk samples of ilmenite-rich pyroclastic
488 samples comprising of glass-rich beads containing microcrystalline olivine (Heiken & McKay,
489 1978). All four of these test spectra were predicted within $\pm 11 \text{ Mg\#}$ of their true composition via
490 feature fitting on laboratory-quality data. When degraded, the samples had similar identification
491 rates for a given SNR and sampling intervals, requiring SNRs ≥ 200 for sampling rates $\leq 25 \text{ nm}$
492 and SNRs ≥ 300 for sampling rates between 30 nm and 60 nm to reach $>90\%$ identification
493 within $\pm 11 \text{ Mg\#}$. These results suggest that compositional predictions derived from feature
494 fitting of IMIR data are accurate for lunar regolith and pyroclastic targets.

495 **5 Conclusions**

496 We investigate the utility of feature fitting on IMIR data for the remote determination of olivine
497 composition and quantitatively identify SNR and sampling rate thresholds required for accurate
498 remote determination of olivine Mg#. We show that:

499

500 1. Olivine absorptions in the IMIR range are easily distinguishable from other lunar-
501 relevant minerals, with 100% of runs detected as olivine across all test spectra for SNRs
502 ≥ 150 and sampling rates $\leq 30 \text{ nm}$.

503

504 2. Comparison of complete band shape via feature fitting is effective at predicting olivine
505 composition using laboratory IMIR data for synthetic, terrestrial, Martian, and lunar
506 samples, with an overall absolute error in compositional prediction of 6.39 Mg\# across all
507 test spectra and 91% of test spectra predicted with $\pm 11 \text{ Mg\#}$ of their true composition.

508

509 3. Applications with more idealized measurements (e.g. minimized spectral mixing over a
510 given pixel; rover/lander spectrometer, laboratory studies) have more lenient data
511 constraints, with some test spectra detected within $\pm 11 \text{ Mg\#}$ for 100% of their true
512 compositions across all runs, despite being degraded to the worst data qualities (30 SNR ,
513 60 nm sampling).

514

- 515 4. SNRs ≥ 200 for sampling rates ≤ 25 nm and SNRs ≥ 300 for larger sampling rates are
516 optimal to accurately estimate the composition of a lunar drive tube sample of ilmenite
517 and glass-rich beads within ± 11 Mg# of their true composition across $\geq 90\%$ of runs.
518

519 **Acknowledgments**

520 This work was supported in part by the National Science Foundation Graduate Research
521 Fellowship under Grant No. 2040433 (S.P.L) and the NASA Postdoctoral Program (C.K.) We
522 thank Michael Bramble for valuable discussion throughout the work.

523 **Data Availability**

524 The data used in this study as well as code files for feature fitting may be accessed at
525 <https://doi.org/10.5281/zenodo.10368444> (Pérez-López et al., 2023).
526

527 **References**

- 528 Burns, R. G. (1970). Crystal field spectra and evidence of cation ordering in olivine minerals.
529 *American Mineralogist*, 55, 1608-1632.
530
- 531 Cañas, C., Pagano, T. S., & Rafol, S. B. (2020). Radiometric performance characterization of the
532 CubeSat Infrared Atmospheric Sounder (CIRAS) High Operating Temperature-Barrier Infrared
533 Detectors (HOT-BIRD). In C. D. Norton, T. S. Pagano, & S. R. Babu (Eds.), *CubeSats and*
534 *SmallSats for Remote Sensing IV* (p. 6). Online Only, United States: SPIE.
535 <https://doi.org/10.1117/12.2570533>
536
- 537 Clark, R.N. (1999). Spectroscopy of Rocks and Minerals, and Principles of Spectroscopy.
538 Manual of Remote Sensing, 3rd. ed.
539
- 540 Clark, R. N., & Roush, T. L. (1984). Reflectance spectroscopy: Quantitative analysis techniques
541 for remote sensing applications. *Journal of Geophysical Research: Solid Earth*, 89(B7), 6329–
542 6340. <https://doi.org/10.1029/JB089iB07p06329>
543
- 544 Clark, R. N., Swayze, G. A., Livo, K. E., Kokaly, R. F., Sutley, S. J., Dalton, J. B., et al. (2003).
545 Imaging spectroscopy: Earth and planetary remote sensing with the USGS Tetracorder and
546 expert systems. *Journal of Geophysical Research: Planets*, 108(E12), 2002JE001847.
547 <https://doi.org/10.1029/2002JE001847>
548
- 549 Clénet, H., Pinet, P., Daydou, Y., Heuripeau, F., Rosemberg, C., Baratoux, D., & Chevrel, S.
550 (2011). A new systematic approach using the Modified Gaussian Model: Insight for the
551 characterization of chemical composition of olivines, pyroxenes and olivine–pyroxene mixtures.
552 *Icarus*, 213(1), 404–422. <https://doi.org/10.1016/j.icarus.2011.03.002>
553
- 554 Dyar, M. D., Sklute, E. C., Menzies, O. N., Bland, P. A., Lindsley, D., Glotch, T., et al. (2009).
555 Spectroscopic characteristics of synthetic olivine: An integrated multi-wavelength and multi-

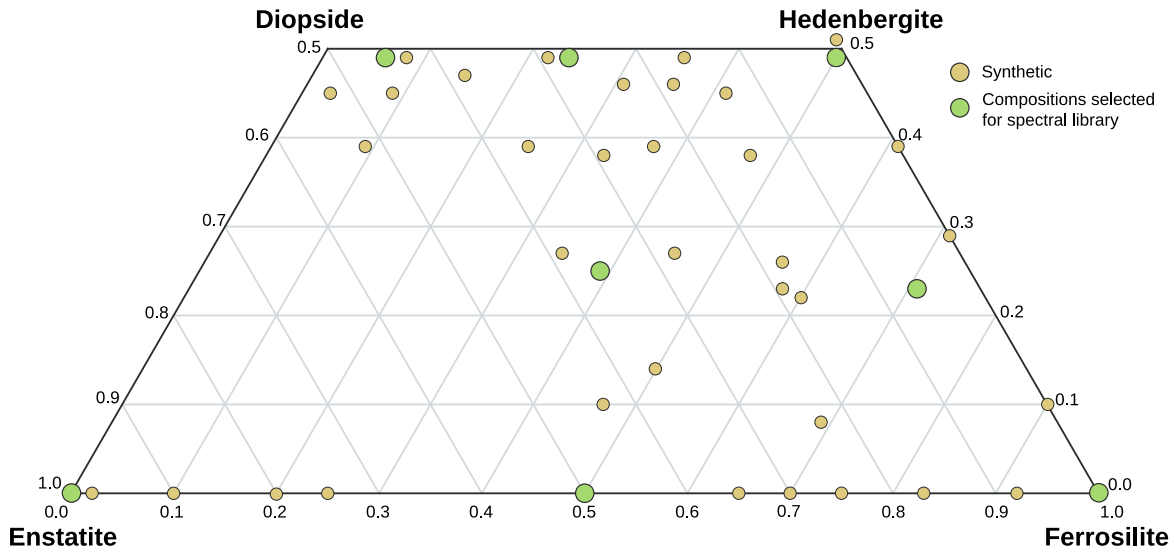
- 556 technique approach. *American Mineralogist*, 94(7), 883–898.
557 <https://doi.org/10.2138/am.2009.3115>
558
- 559 Hamilton, V. E. (2010). Thermal infrared (vibrational) spectroscopy of Mg–Fe olivines: A
560 review and applications to determining the composition of planetary surfaces. *Geochemistry*,
561 70(1), 7–33. <https://doi.org/10.1016/j.chemer.2009.12.005>
562
- 563 Heiken, G., & McKay, D. (1978). Petrology of a sequence of pyroclastic rocks from the valley of
564 Taurus-Littrow (Apollo 17 landing site). *Lunar and Planetary Science Conference Proceedings*,
565 2, 1933–1943. Retrieved from <https://ui.adsabs.harvard.edu/abs/1978LPSC....9.1933H>
566
- 567 Honniball, C. I., Lucey, P. G., Li, S., Shenoy, S., Orlando, T. M., Hibbitts, C. A., et al. (2020).
568 Molecular water detected on the sunlit Moon by SOFIA. *Nature Astronomy*, 5(2), 121–127.
569 <https://doi.org/10.1038/s41550-020-01222-x>
570
- 571 Isaacson, P. J., Pieters, C. M., Besse, S., Clark, R. N., Head, J. W., Klima, R. L., et al. (2011).
572 Remote compositional analysis of lunar olivine-rich lithologies with Moon Mineralogy Mapper
573 (M^3) spectra. *Journal of Geophysical Research*, 116, E00G11.
574 <https://doi.org/10.1029/2010JE003731>
575
- 576 Jackson, C. R. M., Cheek, L. C., Williams, K. B., Hanna, K. D., Pieters, C. M., Parman, S. W., et
577 al. (2014). Visible-infrared spectral properties of iron-bearing aluminated spinel under lunar-like
578 redox conditions. *American Mineralogist*, 99(10), 1821–1833. <https://doi.org/10.2138/am-2014-4793>
579
- 580
581 Klima, R. L., Pieters, C. M., & Dyar, M. D. (2007). Spectroscopy of synthetic Mg-Fe pyroxenes
582 I: Spin-allowed and spin-forbidden crystal field bands in the visible and near-infrared.
583 *Meteoritics & Planetary Science*, 42(2), 235–253. <https://doi.org/10.1111/j.1945-5100.2007.tb00230.x>
584
- 585
586 Koeppen, W. C., & Hamilton, V. E. (2008). Global distribution, composition, and abundance of
587 olivine on the surface of Mars from thermal infrared data. *Journal of Geophysical Research: Planets*, 113(E5), 2007JE002984. <https://doi.org/10.1029/2007JE002984>
588
- 589
590 Kremer, C. H., Mustard, J. F., & Pieters, C. M. (2020). Cross-Over Infrared Spectroscopy: A
591 New Tool for the Remote Determination of Olivine Composition. *Geophysical Research Letters*,
592 47(20), e2020GL089151. <https://doi.org/10.1029/2020GL089151>
593
- 594 Kremer, C. H., Mustard, John. F., & Pieters, C. M. (2023). Intermediate Infrared Spectroscopy of
595 Pyroxene: Determination of Ca-Mg-Fe Composition in the 4–8 Micron Wavelength Range.
596 *Earth and Space Science*, 10(5), e2023EA002828. <https://doi.org/10.1029/2023EA002828>
597
- 598 Kremer, C. H., Mustard, J. F., Pieters, C. M., Gillis-Davis, J. J., & Donaldson Hanna, K.
599 L. (2022). Spectral effects of nano-phase iron and agglutinates in olivine, plagioclase, and lunar
600 soils in the "cross-over" infrared range (4-8 microns). *Presented at the Lunar and Planetary
601 Science Conference LIII*, (p. 2239).

- 602
603 Lane, M. D., Glotch, T. D., Dyar, M. D., Pieters, C. M., Klima, R., Hiroi, T., et al. (2011).
604 Midinfrared spectroscopy of synthetic olivines: Thermal emission, specular and diffuse
605 reflectance, and attenuated total reflectance studies of forsterite to fayalite. *Journal of*
606 *Geophysical Research*, 116(E8), E08010. <https://doi.org/10.1029/2010JE003588>
607
- 608 McCord, T. B., & Clark, R. N. (1979). The Mercury soil: Presence of Fe²⁺. *Journal of*
609 *Geophysical Research: Solid Earth*, 84(B13), 7664–7668.
610 <https://doi.org/10.1029/JB084iB13p07664>
611
- 612 Milliken, R. E., & Mustard, J. F. (2005). Quantifying absolute water content of minerals using
613 near-infrared reflectance spectroscopy. *Journal of Geophysical Research: Planets*, 110(E12),
614 2005JE002534. <https://doi.org/10.1029/2005JE002534>
615
- 616 Nittler, L. R., Starr, R. D., Weider, S. Z., McCoy, T. J., Boynton, W. V., Ebel, D. S., et al.
617 (2011). The Major-Element Composition of Mercury's Surface from MESSENGER X-ray
618 Spectrometry. *Science*, 333(6051), 1847–1850. <https://doi.org/10.1126/science.1211567>
619
- 620 Pérez-López, S., Kremer, C., & Mustard, J. (2023). Dataset and code for ‘Signal to Noise Ratio
621 and Spectral Sampling Constraints on Olivine Detection and Compositional Determination in the
622 Intermediate Infrared Region’ [Data set]. Zenodo. <https://doi.org/10.5281/zenodo.10368444>
623
- 624 Shearer, C. K., Elardo, S. M., Petro, N. E., Borg, L. E., & McCubbin, F. M. (2015). Origin of the
625 lunar highlands Mg-suite: An integrated petrology, geochemistry, chronology, and remote
626 sensing perspective. *American Mineralogist*, 100(1), 294–325. [https://doi.org/10.2138/am-2015-](https://doi.org/10.2138/am-2015-4817)
627 [4817](https://doi.org/10.2138/am-2015-4817)
628
- 629 Stutzki, J. (2006). SOFIA: The Stratospheric Observatory for Infrared Astronomy. In S. Röser
630 (Ed.), *Reviews in Modern Astronomy* (1st ed., pp. 293–314). Wiley.
631 <https://doi.org/10.1002/9783527619030.ch14>
632
- 633 Sunshine, J. M., Pieters, C. M., & Pratt, S. F. (1990). Deconvolution of mineral absorption
634 bands: An improved approach. *Journal of Geophysical Research: Solid Earth*, 95(B5), 6955–
635 6966. <https://doi.org/10.1029/JB095iB05p06955>
636
- 637 Swayze, G. A., Clark, R. N., Goetz, A. F. H., Chrien, T. G., & Gorelick, N. S. (2003). Effects of
638 spectrometer band pass, sampling, and signal-to-noise ratio on spectral identification using the
639 Tetracorder algorithm. *Journal of Geophysical Research: Planets*, 108(E9), 2002JE001975.
640 <https://doi.org/10.1029/2002JE001975>
641
- 642 Ting, D. Z., Soibel, A., Hill, C. J., Keo, S. A., Mumolo, J. M., & Gunapala, S. D. (2012). High
643 operating temperature midwave quantum dot barrier infrared detector (QD-BIRD). In B. F.
644 Andresen, G. F. Fulop, & P. R. Norton (Eds.) (pp. 835332–835332–8). Baltimore, Maryland.
645 <https://doi.org/10.1117/12.920685>
646

647 Wood, J. A., Dickey, J. S., Marvin, U. B., & Powell, B. N. (1970). Lunar Anorthosites. *Science*,
 648 167(3918), 602–604. <https://doi.org/10.1126/science.167.3918.602>

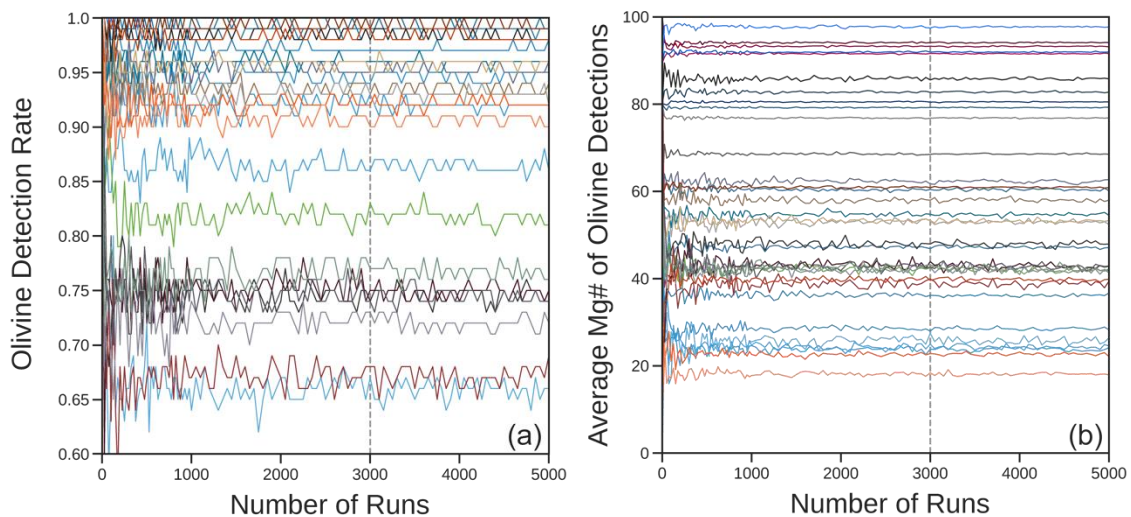
649
 650
 651
 652
 653
 654
 655

Supplementary Figures



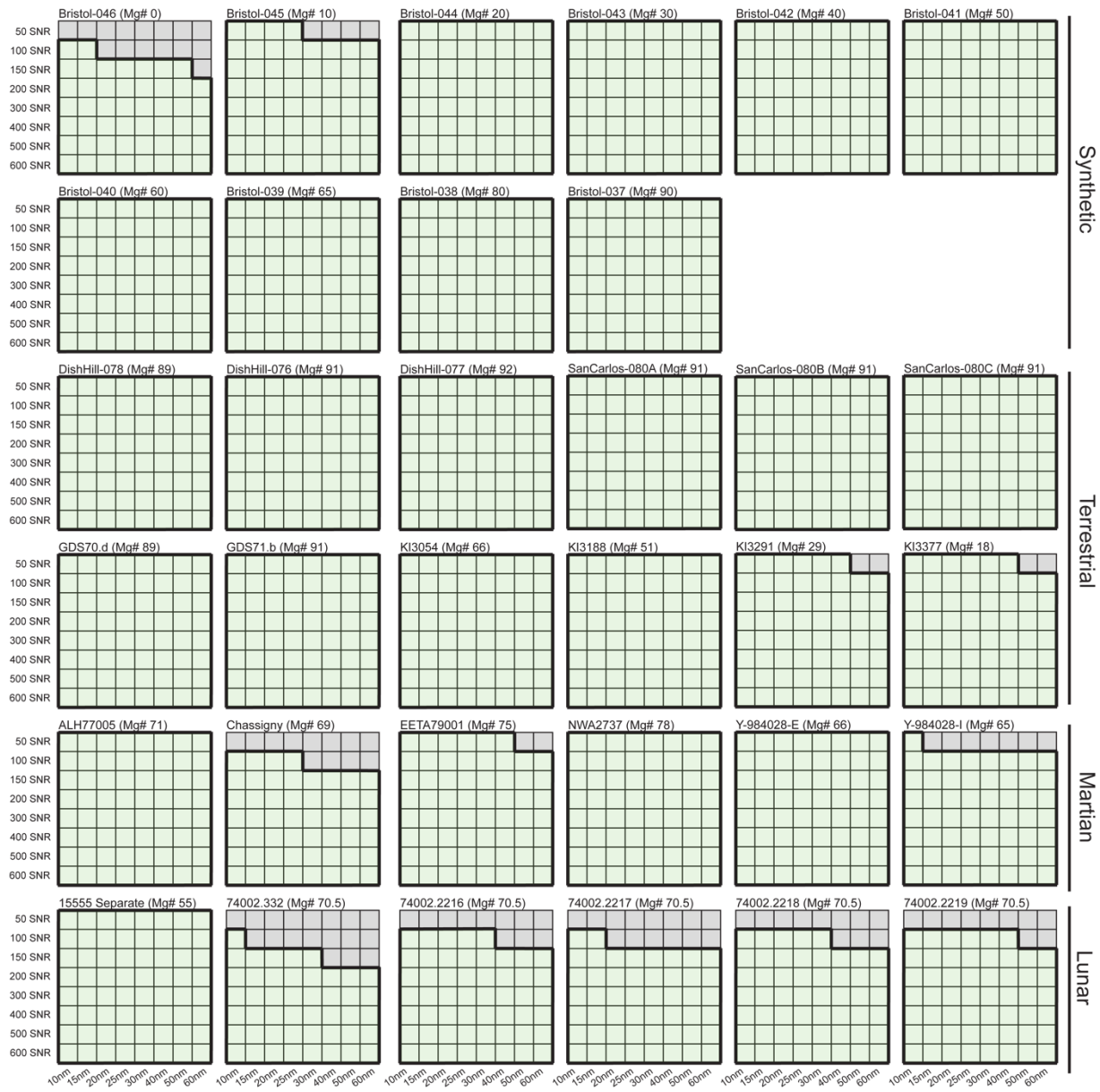
656
 657 **Figure S1.** Synthetic pyroxene suite synthesized by Donald Lindsley (beige markers) and
 658 compositionally representative selection of samples that are included in spectral library (green
 659 markers).

660
 661

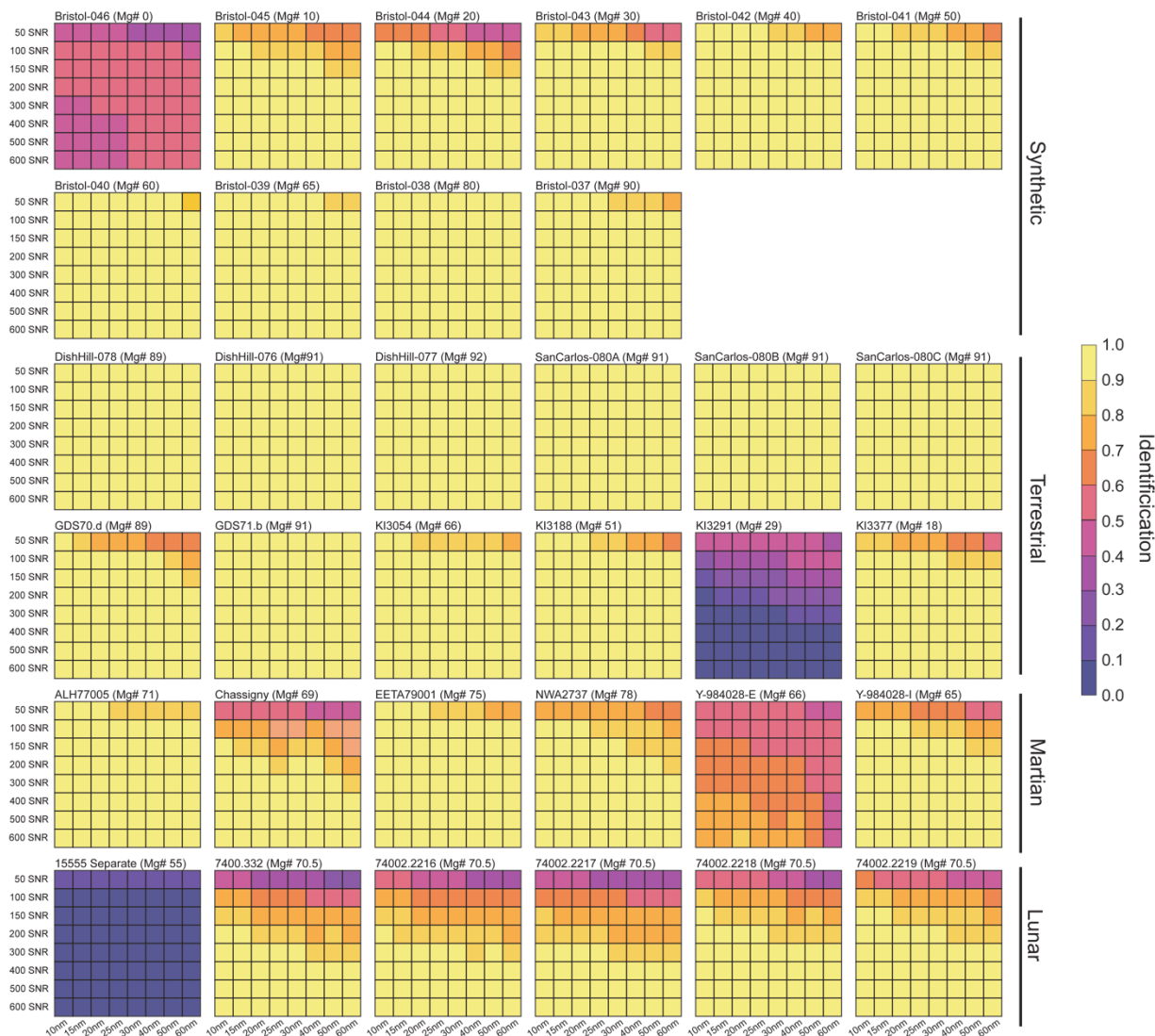


662

663 **Figure S2.** a) Olivine detection rate and b) average Mg# of olivine detections for all test spectra
 664 across and increasing number of runs. Raw data.
 665



666 **Figure S3.** Parameter space required to achieve 100% olivine detection across 3000 runs for all test spectra. Green
 667 grid space denotes data qualities (SNR and sampling rate) where 100% olivine detection was achieved, gray grid
 668 spaces denote data qualities where 100% olivine detection was not achieved. Each grid space represents the result of
 669 3000 feature fits, with each iterations generating a new degraded test spectra with randomly sampled noise defined
 670 by that grid's SNR and resampled to the grid's sampling rate.
 671
 672



673
 674 **Figure S4.** Identification rates within ± 12 Mg# of test spectrum's true composition across a set of feature fitting
 675 runs for all data qualities explored in this study. Each grid space represents the result of 3000 feature fits, with each
 676 iterations generating a new degraded test spectra with randomly sampled noise defined by that grid's SNR and
 677 resampled to the grid's sampling rate.
 678